PHYSICAL REVIEW RESEARCH **4**, 043180 (2022)

Magnon-mediated spin entanglement in the strong-coupling regime

Vasilios Karanikolas,[1,*] Takashi Kuroda,[2] and Jun-ichi Inoue[2]
[1] *International Center for Young Scientists (ICYS), National Institute for Materials Science (NIMS), 1-1 Namiki, Tsukuba, Ibaraki 305-0044, Japan*
[2] *National Institute for Materials Science (NIMS), 1-1 Namiki, Tsukuba, Ibaraki 305-0044, Japan*

(Received 5 April 2022; accepted 27 September 2022; published 12 December 2022)

We present that two spin defects (SDs) can be entangled through a magnon polariton mode, within the strong-coupling regime. The magnon polariton modes are provided by an antiferromagnetic (AFM) $\mathrm{MnF_2}$ layer, where the dispersion of the modes is characterized by the layer's thickness. The macroscopic quantum electrodynamics theory is used to describe the light-matter interactions, where the Green's functions are its core elements. The individual SD relaxes by exciting the magnon polariton modes, exhibiting high enhancement values of the Purcell factor. When two SDs are considered, an oscillatory exchange of population probability is observed between them, a sign of strong-coupling light-matter interactions, where the concurrence value is used to quantify the level of entanglement. The thinner AF layers can potentially be used to promote interactions between multiple spins through long-range coupling. This is a desired feature to fabricate high-demand applications in the fields of quantum measurement and computation.

DOI: 10.1103/PhysRevResearch.4.043180

I. INTRODUCTION

Light-matter interactions are weak, thus the need to store light in a cavity to increase their interaction strength and time. Antiferromagnetic (AFM) materials support magnon polariton modes [1,2] at the gigahertz regime and provide an attractive platform for developing quantum applications. The magnon polariton modes are hybrid modes of the electromagnetic field and the spins of the AFM material; they are confined perpendicularly to the magnet/insulator interface and propagate along it. Nitrogen vacancy spin defects (SDs) in diamond have been used to detect and interact with magnon polariton modes. These modes are launched in magnetic materials in different ways, such as by electrical excitation, microwave excitation, through a scattering center, or by changing the temperature gradient of the magnetic layer [3–6]. The excited state population probability of the SDs undergoes Rabi oscillations due to the excitation from the magnon modes, controlled by the applied signal.

Yttrium iron garnet (YIG) structures, which support magnon polariton modes, are placed in cavities, and when the magnon-cavity resonances are matched, there is an avoided crossing in the scattering (or transmission) spectrum attributed to the light-magnon coupling [7]; although, the scattering (or transmission) spectrum is not a clear way to define the strong-coupling regime. Moreover, the magnon modes are bosonic modes, thus additional nonlinearities are needed to enhance their coupling with light. Hybrid systems, composed from YIG structures and superconducting qubits, both placed in a cavity, operate in the strong-coupling regime [8–10], where extremely low operation temperatures are needed.

The scheme we propose here is based on SDs interacting with magnon polariton modes supported by an AFM layer [11,12]. The SDs are used to store and process the information, while the magnon polariton modes are used to transmit the information between the SDs by enhancing the coupling strength between them. The SD/AFM layer interaction is within the strong-coupling regime, which appears as Rabi oscillations in the population dynamics of the single SD, and population exchange between a pair of SDs. Spin defects are quantum impurities like color centers in diamond or hexagonal boron nitride, where their near field can excite and interact with the magnon polariton modes. A deep understanding of such process is important to develop practical quantum computing and sensor applications.

The interaction of a single SD and a magnetic layer has been investigated with an emphasis on its relaxation, or spin-flip, rate for relaxometry measurements to detect the magnon polariton modes [12–14] or for quantum information applications [15]. Moreover, magnon polariton modes can be tuned by an applied electric field, and such changes can be probed by SDs interacting with these modes [16]. Thus, SDs can be used as sensors to improve dc electric field sensitivity. Also, the relaxation of SDs above an YIG thin layer can be used for sensing nanomechanical forces [17]. Finally, the relaxation of the SDs can be used to probe superconductivity in two-dimensional materials [18]. The entanglement between a pair of SDs has been theoretically investigated considering different nanostructured environments, such as a ferromagnetic

---

[*] karanikolas.vasileios@nims.go.jp

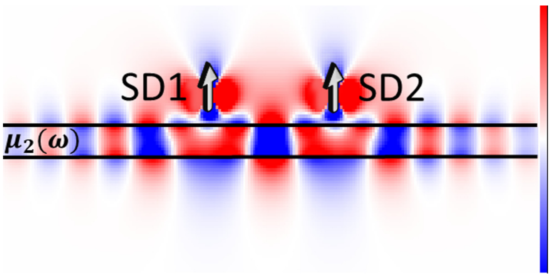

FIG. 1. Contour plot of the real part of the electromagnetic field created by a pair of spin defects, which are entangled through the magnon mode of the antiferromagnetic (AFM) layer. The total SD/AFM layer system is embedded in air.

infinite [19] and finite [19,20] waveguide and a magnetic layer [21–23].

All the above studies are based on density matrix calculations where the Markov approximation has been employed, thus not including memory effects in the entanglement dynamics. Moreover, they only considered the relaxation (of a single SD) and the exchange (between a pair of SDs) rates at a single emission energy.

The Rabi oscillations in the relaxation of a single SD and the population exchange between a pair of SDs have been investigated when interacting through an YIG sphere [24,25], but the structure and material parameters are difficult to approach by the current experimental capabilities. Moreover, in Ref. [26] the Kerr magnons are used to promote the entanglement of distant spin qubits, where the master equation approach is used.

In this paper, the macroscopic quantum electrodynamics (QED) theory [27,28] is used to describe the interaction between a pair of SDs, placed above an AFM layer (Fig. 1). The optical response of the AFM layer is given through the frequency-dependent magnetic permeability $\mu_2(\omega)$ [see Fig. 2(a)], which is connected with the spins' microstructure in the AFM layer. The macroscopic QED theory has been used extensively to describe the relaxation process of quantum systems with electric dipole, while its magnetic counterpart is far less explored [29]. We present that the entanglement dynamics between the two SDs is within the strong-coupling regime, where the two SDs exchange energy coherently. In our analysis the full spectrum to describe the SD/AFM layer coupling is used, where a simple Lorentzian fit widely used is not possible for our case. Moreover, we analyze the dispersion relation of the magnon polariton modes and present how the penetration depth and polariton wavelength influence to the entanglement dynamics between two SDs.

In Sec. II we provide the material parameters of the MnF_2 layer, the dispersion relation of the magnon polariton modes for a single dielectric/AFM layer interface, the macroscopic QED theory used to investigate the entanglement dynamics, and the Green's tensor formalism for the AFM layer. In Sec. III we provide results and a discussion of them, presenting the magnon polariton modes of the AFM layer and introducing the penetration depth of the magnon mode. Then, we present the spin-flip rate of a single SD and the exchange rate between a pair of SDs. We discuss these rate varying different parameters. The population dynamics of a single SD and the population probability exchange between a pair of SDs is presented. For the pair of SDs the entanglement dynamics is presented. Finally, Sec. IV is kept for the conclusions and discussion of the future directions of our research.

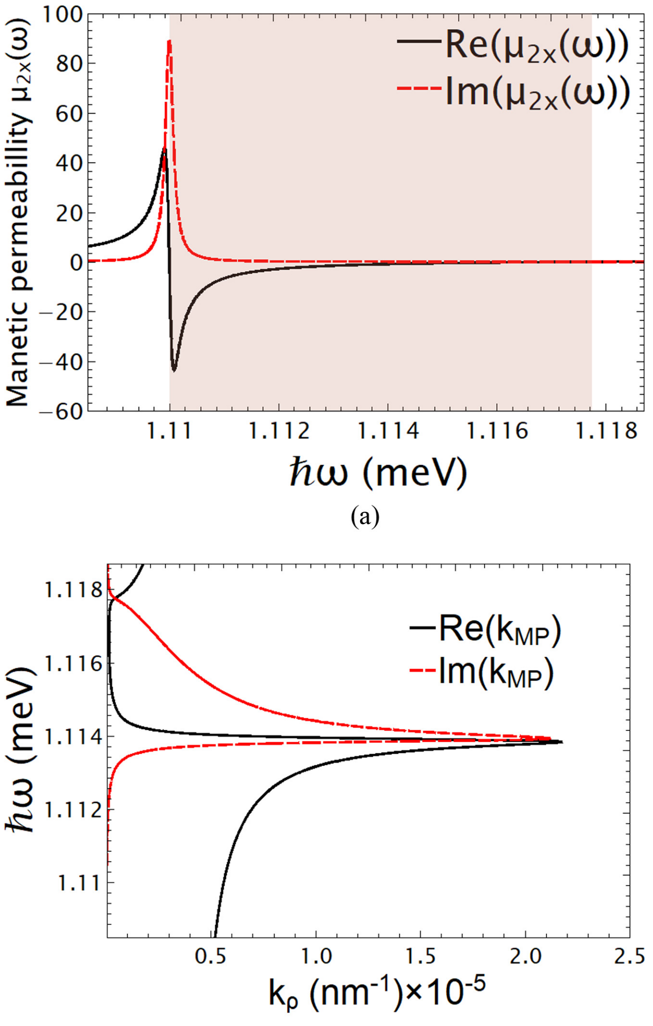

(a)

(b)

FIG. 2. (a) Real and imaginary parts of the magnetic permeability for the antiferromagnetic MnF_2 material; the colored area defines the energy span that $\mathrm{Re}[\mu_{2x}(\omega)] < 0$. (b) Real and imaginary parts of the magnon polariton mode of an AFM/homogeneous dielectric materials interface.

II. MATERIAL PARAMETERS AND THEORETICAL MODEL

A. Magnetic permeability

We focus on an AFM material with uniaxial or easy-axis anisotropy along the z direction, with a rutile crystal structure, a body-centered tetragonal lattice where the magnetic ions occupy the corner, and body-centered positions [30]. In the absence of an external field the spins are arranged in two oppositely directed sublattices, pointing along the easy or c axis. The magnetic properties are described by a spin Hamiltonian consisting of the exchange coupling between nearest neighbors and magnetic anisotropy contributions [31].

The equation of motion of the spin operators is used to define the magnetization components which are connected with the magnetic permeability that describes the macroscopic response of the AFM layer.

Here we focus on $\mathrm{MnF_2}$, which is a well-studied material where spin standing waves have been experimentally observed [1,32,33] and we consider its optical response at 4.2 K. The electromagnetic response of the AFM layer is given by the magnetic permeability $\mu_2(\omega)$, which is described by a Lorentz oscillator model and it is diagonal and uniaxial $\mu_2(\omega) = \mathrm{diag}(\mu_{2x}(\omega), \mu_{2y}(\omega), \mu_{2z})$. In the absence of an external magnetizing field, the diagonal elements are given by

$$\mu_{2x}(\omega) = \mu_{2y}(\omega) = 1 + \frac{2\mu_0 g B_A M_S}{\omega_0^2 - (\omega + i\kappa)^2}, \quad \mu_{2z} = 1, \quad (1)$$

where B_A is the anisotropy field, M_S is the sublattice magnetization, g is the gyromagnetic ratio, and κ is a phenomenological damping parameter. In the approximation of low losses, the resonance frequency ω_0 is given by the expression $\omega_0 = \gamma\sqrt{2B_A B_E + B_A^2} = 1.1\ \mathrm{meV}/\hbar$ ($\lambda_0 = 1.117\,\mathrm{mm}$), where B_E is the exchange field that defines the magnetic field needed to invert neighbor spin pairs and γ is the gyromagnetic ratio. The operation temperature is significantly higher than the millikelvin temperature that the quantum computers, based on superconducting qubits, operate on.

The material losses of the $\mathrm{MnF_2}$ are connected with the $\mathrm{Im}[\mu_{2x}(\omega)]$ and in Fig. 2(a) we observe that at $\hbar\omega_0$ the highest loss is observed; the real part of $\mu_{2x}(\omega)$ is connected with the dispersion of the material and the energy span at which the magnon polariton mode is supported is defined by $\mathrm{Re}[\mu_{2x}(\omega)] < 0$, which is given by the colored area in Fig. 2(a).

B. Single dielectric/AFM interface

It is didactic to first consider the dispersion relation of an AFM/nonmagnetic dielectric single interface, which is given by $k_{\mathrm{MP}} = \frac{\omega}{c}\sqrt{\frac{\mu_1\mu_{2x}}{\mu_1+\mu_{2x}}}$, where μ_{2x} is given by Eq. (1), and is plotted in Fig. 2(b). We observe that the magnon polariton mode, long-range ordered spin waves of the AFM material, is excited when $\mathrm{Re}[(\mu_{2x}(\omega)] < 0$.

We note that the highest magnon wave vector value of $\mathrm{Re}(k_{MP}) = 2.2 \times 10^{-5}\,\mathrm{nm}^{-1}$ is achieved at energy of $\hbar\omega_{MP} = 1.114$ meV where $\mathrm{Re}(\mu_{2x}(\omega_{MP})) = -\mu_1 = -1$ to fulfill the polariton condition. For comparison, the free-space wave vector for the magnon polariton energy $\hbar\omega_{MP}$ is $\omega_{MP}/c = 5.6 \times 10^{-6}\,\mathrm{nm}^{-1}$. Thus, the light line is close to the y axis of Fig. 2(b), away from the magnon polariton light. That means that the magnon polariton modes cannot be excited by direct light illumination. Moreover, we observe the polariton dispersion curve that bends back for energies above $\hbar\omega_{MP}$ due to the material losses, which are connected with the $\mathrm{Im}[\mu_{2x}(\omega)]$.

The magnon polariton modes are confined in the perpendicular dimension in the AFM/nonmagnetic dielectric interface, where $k_z = \sqrt{k_0^2 - k_{MP}^2} \sim ik_{MP}$, considering the AFM permeability $\mu_{2x} = \mu_{2x}' + i\mu_{2x}''$, where for $\mu_{2x} \sim -|\mu_{2x}'| \gg -\mu_1$ the magnon polariton wave vector is imaginary $k_{z1} \sim k_z'' = ik_0\mu_1\sqrt{|\mu_{2x}'|}/|\mu_{2x}'|$, thus the out-of-plane electromagnetic field away from the interface $\sim\exp(ik_z z)$ is decaying. This physical condition holds for the magnon polariton modes of the AFM layer.

C. Macroscopic quantum electrodynamics

The Zeeman Hamiltonian describes the interaction of multiple SDs in a magnetic environment and is given by [24,28,29]

$$\hat{H} = \hat{H}_0 + \hat{H}_{\mathrm{int}}, \quad (2)$$

where $\hat{H}_0$ is the free-space Hamiltonian of the SDs and the bosonic field operator, given by

$$\hat{H}_0 = \sum_j \hbar\omega_1 |\uparrow_j\rangle\langle\uparrow_j| + \int d^3r \int d\omega\, \hbar\omega \hat{\mathbf{f}}_m^\dagger(\mathbf{r}, \omega)\cdot\hat{\mathbf{f}}_m(\mathbf{r}, \omega), \quad (3)$$

where the summation is over the multiple SDs. The index j gives the number of the SD that is in the state $|\uparrow\rangle$, at position $\mathbf{r}_j$, and all the other SDs are in state $|\downarrow\rangle$; the SDs considered are identical with the same transition energy, $\hbar\omega_1$, and magnetic dipole moment. The bosonic field operator $\hat{\mathbf{f}}_m(\mathbf{r}, \omega)$ describes all the electromagnetic modes available in the system, including the magnon polariton modes.

The interaction between the multiple SDs, placed at $\mathbf{r}_j$, with the magnetic field $\hat{\mathbf{B}}(\mathbf{r}_j)$, considered at the position of the relevant SD, is given by the Zeeman Hamiltonian,

$$\hat{H}_{\mathrm{int}} = -\sum_j \hat{\mu}_j \cdot \hat{\mathbf{B}}_j(\mathbf{r}_j), \quad (4)$$

where $\hat{\mu}_j = \frac{\mu_B g}{\hbar}\hat{\mathbf{S}}_j$, μ_B is the Bohr magnetron and $\hat{\mathbf{S}}_j = \frac{\hbar}{2}\hat{\sigma}_j$ is the spin angular momentum operator, $g \simeq 2.000\,02$ is the spectroscopic splitting factor, and $\hat{\mu}_j = g\mu_B/2[\hat{\sigma}_x, \hat{\sigma}_y, \hat{\sigma}_z]_j$ is the transition magnetic dipole moment of the j SD.

Due to the form of the transition dipole moment $\hat{\mu}_j$, there are no z magnetic transitions for the SDs. So, in the rest of the paper we focus on x-oriented transition dipole moments, where for the j SD have the form $\hat{\mu}_j = \mu_B g/2[|\downarrow_j\rangle\langle\uparrow_j| + \mathrm{H.c.}]$ [2,34–36]. We consider one of the SDs to be excited above an AFM layer of thickness D; then it can relax to the ground state by emitting a photon or exciting the magnon polariton mode, indicated by the spin-flip rate of the SD. If there is nearby a second SD interacting with the excited SD, then an exchange of population through the magnon polariton mode can be observed.

The magnetic field operator is given by the expression [37]

$$\hat{\mathbf{B}}(\mathbf{r}, \omega) = \mu_0 \int d^3r' \{\nabla_r \times \mathfrak{G}(\mathbf{r}', \mathbf{r}, \omega)\} \cdot \{\nabla_{r'} \times \hat{\mathbf{M}}_N(\mathbf{r}', \omega)\}, \quad (5)$$

where $\hat{\mathbf{M}}_N(\mathbf{r}, \omega)$ is the Langevin noise magnetization operator that accounts for the lossy AFM layer [27]. The form of $\hat{\mathbf{M}}_N(\mathbf{r}, \omega)$ is connected with the imaginary part of the magnetic permeability $\mathrm{Im}[\mu(\mathbf{r}, \omega)]$ that describes the electromagnetic response of the AFM material [38]. The magnetization is given in terms of the bosonic vector field $\hat{\mathbf{f}}_m(\mathbf{r}, \omega)$ through the equation

$$\mathbf{M}_N(\mathbf{r}, \omega) = \sqrt{-\frac{\hbar k_0}{\pi}\mathrm{Im}\mu(\mathbf{r}, \omega)^{-1}}\,\hat{\mathbf{f}}_m(\mathbf{r}, \omega), \quad (6)$$

where $k_0 = \omega/c$, $\mathfrak{G}(\mathbf{r}', \mathbf{r}, \omega)$ is the Green's tensor, a 3×3 matrix with Green's function entries; in the end of this section we present how to calculate this quantity for an AFM layer.

To describe the light-matter interactions in the time domain, we start by considering a single SD, $j = 1$, and placed at $\mathbf{r}_1$, in the one-state excitation [39]

$$|\psi(t)\rangle = c_1(t)e^{-i\omega_1 t}|\uparrow, 0_{\mathbf{r}_1,\omega}\rangle + \int d\mathbf{r}\int d\omega\, C(\mathbf{r}, \omega, t)e^{-i\omega t}|\downarrow, 1_{\mathbf{r},\omega}\rangle, \tag{7}$$

where $|c_1|^2$ is the probability for the SD to be at the excited state and $|C(\mathbf{r}, \omega, t)|^2$ is the spatial probability distribution of the electromagnetic modes. From the Schrödinger equation, we focus on the expression for the excited state probability of the SD,

$$\frac{dc_1(t)}{dt} = i\mu_0 \int dr' \int d\omega \sqrt{-\frac{\hbar k_0}{\pi}\mathrm{Im}\mu(\mathbf{r}', \omega)^{-1}} \times C(\mathbf{r}', \omega, t)e^{-i(\omega-\omega_1)t}\mathfrak{I}(\mathbf{r}', \mathbf{r}_1, \omega), \tag{8}$$

where $\mathfrak{I}(\mathbf{r}_2, \mathbf{r}_1, \omega) = \nabla_1 \times \nabla_2 \times \mathfrak{G}(\mathbf{r}_2, \mathbf{r}_1, \omega)$ is a tensor that gives the electromagnetic response of the AFM layer at position $\mathbf{r}_2$ to a magnetic dipole excitation at position $\mathbf{r}_1$. For the field probability density

$$\frac{dC(\mathbf{r}, \omega, t)}{dt} = -i\sqrt{-\frac{\hbar}{\mu_0\pi}\mathrm{Im}\mu(\mathbf{r}, \omega)^{-1}} \times c_1(t)e^{i(\omega-\omega_1)t}\mathfrak{I}^*(\mathbf{r}, \mathbf{r}_1, \omega), \tag{9}$$

which we formally integrate and get the expression

$$C(\mathbf{r}, \omega, t) = i\mu_0\sqrt{-\frac{\hbar}{\mu_0\pi}\mathrm{Im}\mu(\mathbf{r}, \omega)^{-1}}\mathfrak{I}^*(\mathbf{r}, \mathbf{r}_1, \omega) \times \int_0^t dt' c_1(t')e^{i(\omega-\omega_1)t'}, \tag{10}$$

which we plug into (8) to extract the integrodifferential equation for the population dynamics of the excited state of the SD:

$$\frac{dc_1(t)}{dt} = i\int_0^t K(t-t')c_1(t')dt', \tag{11}$$

where the kernel of the equation is given by

$$K(\tau) = ie^{i\omega_1\tau}\int_0^\infty J(\omega)e^{-i\omega\tau}d\omega \tag{12}$$

and $J(\omega_1, \omega, \mathbf{r}_1) = \frac{\Gamma_B(\omega_1)}{2\pi}\Gamma_x(\omega, \mathbf{r}_1)$ is the spectral density, where $\hbar\omega_1$ is the energy difference between the ground and the excited states of the SD, Γ_B is the free-space spin-flip rate of the SD, and Γ_x is the spin-flip rate in the presence of the AFM layer and its full form is given in Sec. II D. The system of two identical SDs, that are placed at $\mathbf{r}_1$ and $\mathbf{r}_2$, is described by the state [40]

$$|\psi(t)\rangle = c_1(t)e^{-i\omega_1 t}|\uparrow_1, \downarrow_2, 0_{\mathbf{r_1},\omega}\rangle + c_2(t) \times e^{-i\omega_1 t}|\downarrow_1, \uparrow_2, 0_{\mathbf{r_2},\omega}\rangle + \int d\mathbf{r}\int d\omega\, C(\mathbf{r}, \omega, t) \times e^{-i\omega t}|\downarrow_1, \downarrow_2, 1_{\mathbf{r},\omega}\rangle, \tag{13}$$

where in $|1, 2, \text{field}\rangle$ the third entry describes the number of electromagnetic excitations in the system, and the first and second indices describe the ↑ or ↓ state of SDs 1 and 2, respectively. After a few algebraic calculations, similar to the case of a single SD discussed earlier, we extract the system of integrodifferential equations,

$$\frac{dc_1(t)}{dt} = i\int_0^t K(t-t')c_1(t')dt' + i\int_0^t K_{12}(t-t')c_2(t')dt', \tag{14a}$$

$$\frac{dc_2(t)}{dt} = i\int_0^t K_{12}(t-t')c_1(t')dt' + i\int_0^t K(t-t')c_2(t')dt', \tag{14b}$$

where $|c_i(t)|^2$ $(i = 1, 2)$ is the population density of the excited state of each SD.

The kernel $K(\tau)$ of Eq. [14] describes the interaction of the individual SDs with the AFM layer and is given by $K(\tau) = ie^{i\omega_1\tau}\int_0^\infty J(\mathbf{r}_j, \omega)/2\pi e^{-i\omega\tau}d\omega$, $j = 1, 2$ for the position of each SD; $J = 1/[2\pi]\Gamma_B\tilde{\Gamma}_x$ is the spectral density and has the same value for both SDs because they are placed at the same distance above the AFM layer.

The interaction between two SDs is given by the kernel $K_{12}(\tau) = ie^{i\omega_1\tau}\int_0^\infty J_{12}(\mathbf{r}_1, \mathbf{r}_2, \omega)/2\pi e^{-i\omega\tau}d\omega$, where $J_{12} = 1/[2\pi]\Gamma_B\tilde{\Gamma}_x^{12}$ is the exchange energy rate between the two SDs, respectively. In this paper we consider SDs that are identical, with the same transition energy $\hbar\omega_1$ and are placed at the same distance z_{SD} above the AFM layer of thickness D at an in-plane distance ρ.

D. Green's tensor formalism for an antiferromagnetic layer

The Green's tensor satisfies the Helmholtz equation,

$$\nabla \times \frac{1}{\mu(\mathbf{r_1}, \omega)}\nabla \times \mathfrak{G}(\mathbf{r_2}, \mathbf{r_1}, \omega) - \frac{\omega^2}{c^2}\varepsilon(\mathbf{r_1}, \omega)\mathfrak{G}(\mathbf{r_2}, \mathbf{r_1}, \omega) = \delta(\mathbf{r_2} - \mathbf{r_1}), \tag{15}$$

where $\mu(\mathbf{r_1}, \omega)$ is the magnetic permeability and $\varepsilon(\mathbf{r_1}, \omega)$ is the dielectric permittivity of the media the SD is embedded within. The method of scattering superposition is used to calculate the Green's tensor $\mathfrak{G}(\mathbf{r_2}, \mathbf{s_1}, \omega)$, where it splits into two parts:

$$\mathfrak{G}(\mathbf{r_2}, \mathbf{r_1}, \omega) = \mathfrak{G}_h(\mathbf{r_2}, \mathbf{r_1}, \omega) + \mathfrak{G}_s(\mathbf{r_2}, \mathbf{r_1}, \omega), \tag{16}$$

$\mathfrak{G}_h(\mathbf{r_1}, \mathbf{r_2}, \omega)$ is the homogeneous part that accounts for direct interaction between the source and target point at $\mathbf{r_1}$ and $\mathbf{r_2}$, respectively, and is nonzero when both points are in the same media. $\mathfrak{G}_s(\mathbf{r_2}, \mathbf{r_1}, \omega)$ is the scattering part, is always present, and accounts for the multiple reflections and transmissions taking place at the interfaces.

The general form of the scattering part of the Green's tensor has the form

$$\mathfrak{G}_s(\mathbf{r_i}, \mathbf{r_j}, \omega) = \frac{i}{8\pi^2}\int d^2k_\rho \frac{1}{k_{zj}k_\rho^2}\sum_T R_T^{\pm(ij)\pm}\mathbf{T}(\mathbf{k}_\rho, \pm k_{zi}, \mathbf{r_i}) \otimes \mathbf{T}^*(\mathbf{k}_\rho, \pm k_{zj}, \mathbf{r_j}); \tag{17}$$

a summation is implied for each pair of ± indices. These indices show the direction of propagation of the electromagnetic modes, the first index for the target point and the second for the position of the excitation source. Also the summation over $\mathbf{T}$ is over the $\mathbf{M}$ and $\mathbf{N}$ modes which are connected with the transverse electric and transverse magnetic modes, respectively.

We focus on the case in which the SDs are placed above an AFM layer, of thickness D, embedded in a homogeneous nonmagnetic, $\mu_1 = 1$, dielectric media with dielectric permittivity $\varepsilon_1 = 1$, free space. The boundary conditions imposed on the system of multilayers are the continuity condition and the radiation condition. The two conditions are imposed to the two interfaces $z_1 = D$ and $z_2 = 0$,

$$\hat{\mathbf{z}} \times [\mathfrak{G}^{(i+1,1)}(\mathbf{r_2}, \mathbf{r_1}, \omega) - \mathfrak{G}^{(i,1)}(\mathbf{r_2}, \mathbf{r_1}, \omega)]|_{z=z_i} = 0, \tag{18a}$$

$$\hat{\mathbf{z}} \times \left[\frac{1}{\mu_{i+1}} \nabla \times \mathfrak{G}^{(i+1,1)}(\mathbf{r_2}, \mathbf{r_1}, \omega) - \frac{1}{\mu_i} \nabla \times \mathfrak{G}^{(i,1)}(\mathbf{r_2}, \mathbf{r_1}, \omega)\right]\Bigg|_{z=z_i} = 0, \tag{18b}$$

with $i = 1, 2$ denoting the upper and lower interfaces and μ_i the magnetic permeability tensor of each medium. The transverse electric and magnetic modes are given by $\mathbf{M}(\mathbf{k}, \mathbf{r}) = i\mathbf{k} \times \hat{z}e^{i\mathbf{k}\cdot\mathbf{r}}$ and $\mathbf{N}(\mathbf{k}, \mathbf{r}) = i\frac{1}{k}\mathbf{k} \times \mathbf{k} \times \hat{z}e^{i\mathbf{k}\cdot\mathbf{r}}$, respectively. Where $\mathbf{k} = (\mathbf{k}_\rho, k_z)$ is the total wave vector, $\mathbf{k}_\rho = \mathbf{i}k_x + \mathbf{j}k_y$ is the in-plane wave vector and k_z is the out-of-plane wave vector.

By applying the boundary equations at the $z = 0$ and $z = D$ interfaces, defined by an AFM layer with thickness D placed in a homogeneous dielectric environment, an inhomogeneous system of four equations is extracted, which has four unknown quantities, the generalized R_M^{i1} and R_N^{i1} coefficients, for $i = 1, 2, 3$. These coefficients uniquely determine the problem under consideration through the exact knowledge of the scattering part of the Green's tensor $\mathfrak{G}_s(\mathbf{r_2}, \mathbf{r_1}, \omega)$. In order to find the form of the generalized coefficients, a matrix equation system is solved for the transverse electric and transverse magnetic modes,

$$\Delta_{M(N)} \cdot \boldsymbol{R}_{M(N)} = \boldsymbol{V}_{M(N)}, \tag{19}$$

where $\Delta_{M(N)}$ are the characteristic matrices of the system of equations from the boundary conditions at the two interfaces. $\boldsymbol{R}_{M(N)}$ are the columns of the generalized reflection coefficients and $\boldsymbol{V}_{M(N)}$ are the free term vectors whose elements are given by the homogeneous part of the Green's tensor.

$$\boldsymbol{R}_M = \begin{pmatrix} R_M^{+(11)-} \\ R_M^{+(21)-} \\ R_M^{-(21)-} \\ R_M^{-(31)-} \end{pmatrix}, \quad \boldsymbol{R}_N = \begin{pmatrix} R_N^{+(11)-} \\ R_N^{+(21)-} \\ R_N^{-(21)-} \\ R_N^{-(31)-} \end{pmatrix}; \tag{20}$$

the free-space terms are given by

$$\boldsymbol{V}_M = \begin{pmatrix} e^{-ik_{z1}D} \\ \frac{k_{z1}}{\mu_1}e^{-ik_{z1}D} \\ 0 \\ 0 \end{pmatrix}, \quad \boldsymbol{V}_N = \begin{pmatrix} \frac{k_{z1}}{k_1}e^{-ik_{z1}D} \\ -\frac{k_1}{\mu_1}e^{-ik_{z1}D} \\ 0 \\ 0 \end{pmatrix}, \tag{21}$$

and the characteristic matrices have the form

$$\Delta_M = \begin{pmatrix} e^{ik_{z1}D} & -e^{ik_{z2}^oD} & -e^{-ik_{z2}^oD} & 0 \\ \frac{k_{z1}}{\mu_1}e^{ik_{z1}D} & -\frac{k_{z2}^o}{\mu_{2x}}e^{ik_{z2}^oD} & \frac{k_{z2}^o}{\mu_{2x}}e^{-ik_{z2}^oD} & 0 \\ 0 & 1 & 1 & -1 \\ 0 & \frac{k_{z2}^o}{\mu_{2x}} & -\frac{k_{z2}^o}{\mu_{2x}} & \frac{k_{z3}}{\mu_3} \end{pmatrix}, \tag{22a}$$

$$\Delta_N = \begin{pmatrix} \frac{k_{z1}}{k_1}e^{ik_{z1}D} & -\frac{k_{z2}^e}{k_2}e^{ik_{z2}^eD} & \frac{k_{z2}^e}{k_2}e^{-ik_{z2}^eD} & 0 \\ \frac{k_1}{\mu_1}e^{ik_{z1}D} & -\frac{k_2}{\mu_{2x}}e^{ik_{z2}^eD} & -\frac{k_2}{\mu_{2x}}e^{-ik_{z2}^eD} & 0 \\ 0 & \frac{k_{z2}^e}{k_2} & -\frac{k_{z2}^e}{k_2} & \frac{k_{z3}}{k_3} \\ 0 & \frac{k_2}{\mu_{2x}} & \frac{k_2}{\mu_{2x}} & -\frac{k_3}{\mu_3} \end{pmatrix}, \tag{22b}$$

where $k_{zi} = \sqrt{k_i^2 - k_\rho^2}$, $k_i = \omega/c\sqrt{\varepsilon_i\mu_i}$ for $i = 1, 3$, and k_ρ is the in-plane wave vector. Within the AFM layer ordinary and extraordinary modes are allowed [1], where $k_{z2}^o = \sqrt{k_2^2 - k_\rho^2}$ and $k_{z2}^e = \sqrt{k_2^2 - \mu_{2x}/\mu_{2z}k_\rho^2}$, respectively, for $k_2 = \omega/c\sqrt{\varepsilon_2\mu_{2z}}$.

After the above analysis we can now calculate the spectral densities connected with the spin-flip (for the single SD) and exchange (between two SDs) rates through the knowledge of the scattering part of the Green's tensor. We remind the reader that the Green's tensor needs to be translated to the $\mathfrak{I}$ tensor through the expression $\mathfrak{I}(\mathbf{r_2}, \mathbf{r_1}, \omega) = \nabla_{\mathbf{r_2}} \times \nabla_{\mathbf{r_1}} \times \mathfrak{G}(\mathbf{r_2}, \mathbf{r_1}, \omega)$; $\mathfrak{I}$ gives the electromagnetic response of the geometry under consideration to a magnetic dipole excitation. Considering a SD placed at $\mathbf{r_1} = (0, 0, z_{\mathrm{SD}})$ distance above the AFM layer, with a magnetic transition dipole moment along x, the spin-flip rate is given by [37]

$$\frac{\Gamma_x(\mathbf{r_1}, \omega)}{\Gamma_B} = \sqrt{\varepsilon_1\mu_1} + \frac{6\pi c}{\omega}\mathrm{Im}[\mathfrak{I}_{xx}(\mathbf{r_1}, \mathbf{r_1}, \omega)], \tag{23}$$

which equation is extracted using the linear fluctuation-dissipation theorem, written in terms of the dyadic Green's tensor for the macroscopic quantum electrodynamics [27]. Through the relation $2\pi J = \Gamma_B\Gamma_x$ the normalized spectral density is given by

$$\frac{2\pi J(\mathbf{r_1}, \omega)}{\Gamma_B} = \sqrt{\varepsilon_1\mu_1} + \frac{3c}{4\omega}\mathrm{Im}\left[i\int_0^\infty \mathrm{d}k_\rho \frac{k_\rho k_1^2}{k_{z1}}\left(R_N^{+11-} - \frac{k_{z1}^2}{k_1^2}R_M^{+11-}\right)e^{2ik_{z1}z_{SD}}\right]. \tag{24}$$

Similarly the exchange rate between a pair of SDs, placed at $\mathbf{r}_1 = (0, 0, z_{\mathrm{SD}})$ and $\mathbf{r}_2 = (\rho, z_{\mathrm{SD}})$, is given by

$$\frac{2\pi J_{12}(\omega, \mathbf{r})}{\Gamma_B} = \frac{3c}{2\omega}\mathrm{Im}\left\{i\int_0^\infty dk_\rho \frac{k_\rho k_1^2}{k_{z1}}\left[\left(\frac{J_1(k_\rho\rho)}{k_\rho\rho} - J_2(k_\rho\rho)\right)R_N^{+11-} - \frac{J_1(k_\rho\rho)}{k_\rho\rho}\frac{k_{z1}^2}{k_1^2}R_M^{+11-}\right]e^{2ik_{z1}z_{SD}}\right\}, \tag{25}$$

where $J_i(r)$, for $i = 1, 2$, are the Bessel functions, and ρ and k_ρ are the in-plane distance between the two SDs and the in-plane wave vector, respectively. Γ_B is the reference spin-flip rate of the individual SD, $\Gamma_B = \mu_0\frac{\mu_B^2 g_s^2}{3\pi\hbar}\frac{\omega^3}{c^3}$, where $\frac{\mu_0\mu_B^2}{\hbar} =$

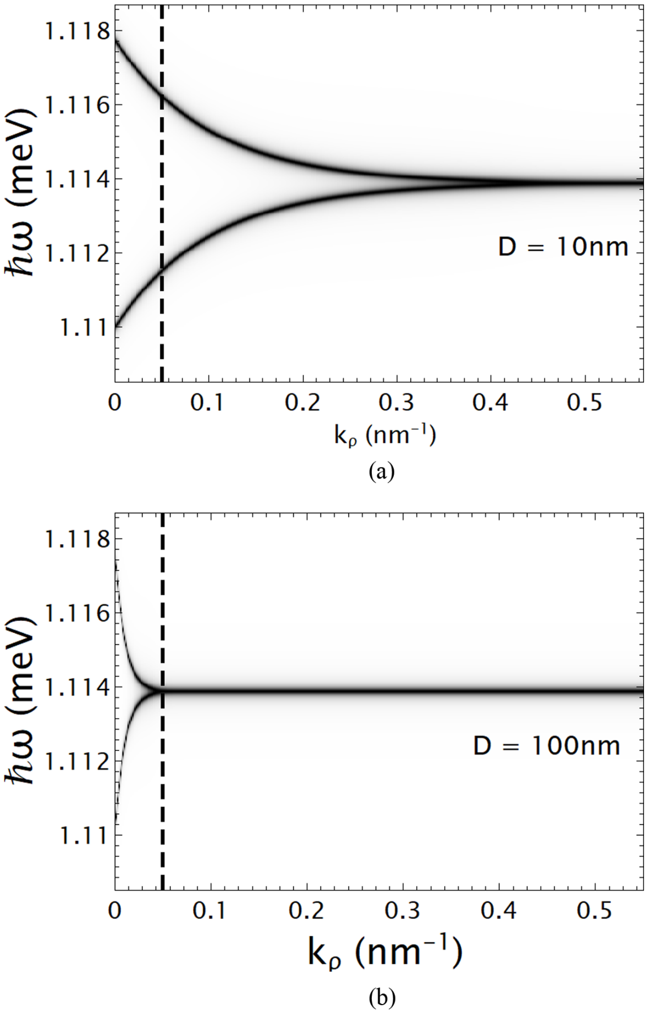

(a)

(b)

FIG. 3. Dispersion relation $\omega(k_{\text{MP}})$ of the antiferromagnetic layer considering two different thicknesses (a) 10 nm and (b) 100 nm. The dashed lines define the $k_\rho = 0.05\ \text{nm}^{-1}$ connected with the penetration depth of 10 nm.

$1.025\frac{\text{nm}}{\text{ns}}$ and $g_s \simeq 2$ [24]. The unit of Γ_B is $[\Gamma_B] = \text{ns}^{-1}\,\text{nm}^{-2}$. Here $R^{+11-}_{N(M)}$ are the generalized Fresnel coefficients, which can be calculated through Eq. (19).

III. RESULTS AND DISCUSSION

In Figs. 3(a) and 3(b) the dispersion relation $\omega(k_{\text{MP}})$ of a freestanding MnFe$_2$ AFM layer is presented for two thicknesses: (a) 10 nm and (b) 100 nm. The contour plots of Fig. 3 present the normalized values of the integrand of the Green's tensor, $\text{Imag}[d\mathfrak{G}(\mathbf{r}, \mathbf{r}, \omega)/dk_\rho]$, for which an exact value is not important to describe the physics governing the magnon polariton modes; the magnon polariton $\omega(k_{\text{MP}})$ curve is given by the black color. The width of the dispersion curve is connected with the MnFe$_2$ material loss $\hbar\kappa = 8.7 \times 10^{-5}$ meV, Eq. (1). The dispersion relation presents two branches: the symmetric and antisymmetric transverse electric/magnetic modes. As the thickness D of the AFM layer is increased, the two modes overlap for smaller values of the in-plane wave vector, k_ρ, compared to the thinner one. The magnon polariton modes are supported at energies above $\hbar\omega_0$, where $\mu_{2x}(\omega) < 0$. The dispersion relation curve of the magnon polariton modes is away from the light line, thus they cannot be excited by direct light illumination due to momentum mismatch. The near field of the SD can efficiently excite the magnon polariton modes of the AFM layer, when placed within the penetration depth δ of the magnon polariton mode, $\delta = 1/\text{Im}(2k_z)$, and for $k_z = \sqrt{k_0^2 - k_{\text{MP}}^2} \simeq ik_{\text{MP}}$ we get $\delta = 1/(2k_{\text{MP}})$, which ultimately characterizes the interaction length between the SD/AFM layer.

In Fig. 4 we present contour plots of the spin flip of a SD and the exchange rate between a pair of SDs when interacting through the AFM layer, where we vary the emission energy and the position of the SDs. Two thicknesses are considered. Figures 4(a), 4(c) and 4(e): $D = 10$ nm; Figs. 4(b), 4(d) and 4(f): $D = 100$ nm.

We start the discussion by focusing on the spin-flip rate of a single SD [Figs. 4(a) and 4(b)]. We observe that for $D = 10$ nm there are two peaks in the $J(\mathbf{r}, \omega)$ spectrum, while for $D = 100$ nm there is only a single peak. This effect can be explained with the help of the dispersion relation of Fig. 3; for $D = 10$ nm the dispersion relation presents two branches [Fig. 3(a)] for high values of the in-plane wave vectors k_{MP}, meaning that the two polariton modes are accessible for small SD/AFM layer separations. While for $D = 100$ nm, the two branches collapse to a single branch at smaller k_{MP} values, presenting a single peak in the spin-flip spectrum of the SD. The penetration depth for a SD that is placed 10 nm away from the AFM layer is connected with the wave-vector value of $k_{\text{MP}} = 0.05\ \text{nm}^{-1}$, which is shown by the dashed line in Fig. 3, and the energies it crosses the $\omega(k_{\text{MP}})$ curve that give the energy peaks of the J spectrum observed in Figs. 4(a) and 4(b).

A pair of SDs exchange energy with a rate $J_{12}(\mathbf{r}_1, \mathbf{r}_2, \omega)$, and in Figs. 4(c) and 4(d) contour plots are presented for varying the transition energy of the SDs and the z_{SD} SD/AFM layer separation distance. In Fig. 4(c) the in-plane distance between the SDs is 15 nm and we observe that J_{12} presents multiple peaks and troughs. The reason for such behavior is that for varying $\hbar\omega$ the magnon polariton modes propagate with different polariton wavelengths $\lambda_{\text{MP}} = 2\pi/k_{\text{MP}}$ along the AFM layer, leading to the oscillatory features in Fig. 4(c), where k_{MP} is the magnon polariton wave vector presented in Fig. 3. On the other hand, in Fig. 4(d) the separation distance is 25 nm and we observe that for a given SD/AFM layer separation there are less peaks and troughs concentrated close to the transition energy of $\hbar\omega = 1.11388$ meV; again this effect is connected with the magnon polariton resonance energy and the relevant wavelength. The thicker the AFM layer the closer the magnon polariton dispersion relation to the single AFM/dielectric interface [Fig. 2(b)]. Thus, as anticipated from the comparison with plasmonic materials, the thicker AFM layer behaves as a single interface geometry. The different thicknesses of the AFM layer support confined modes with different polariton wavelength; hence, we focus on separation distances between the SDs that are connected with the highest value of the interaction strength between them.

To further investigate the oscillatory behavior of the exchange rate J_{12} between a pair of SDs, we consider a

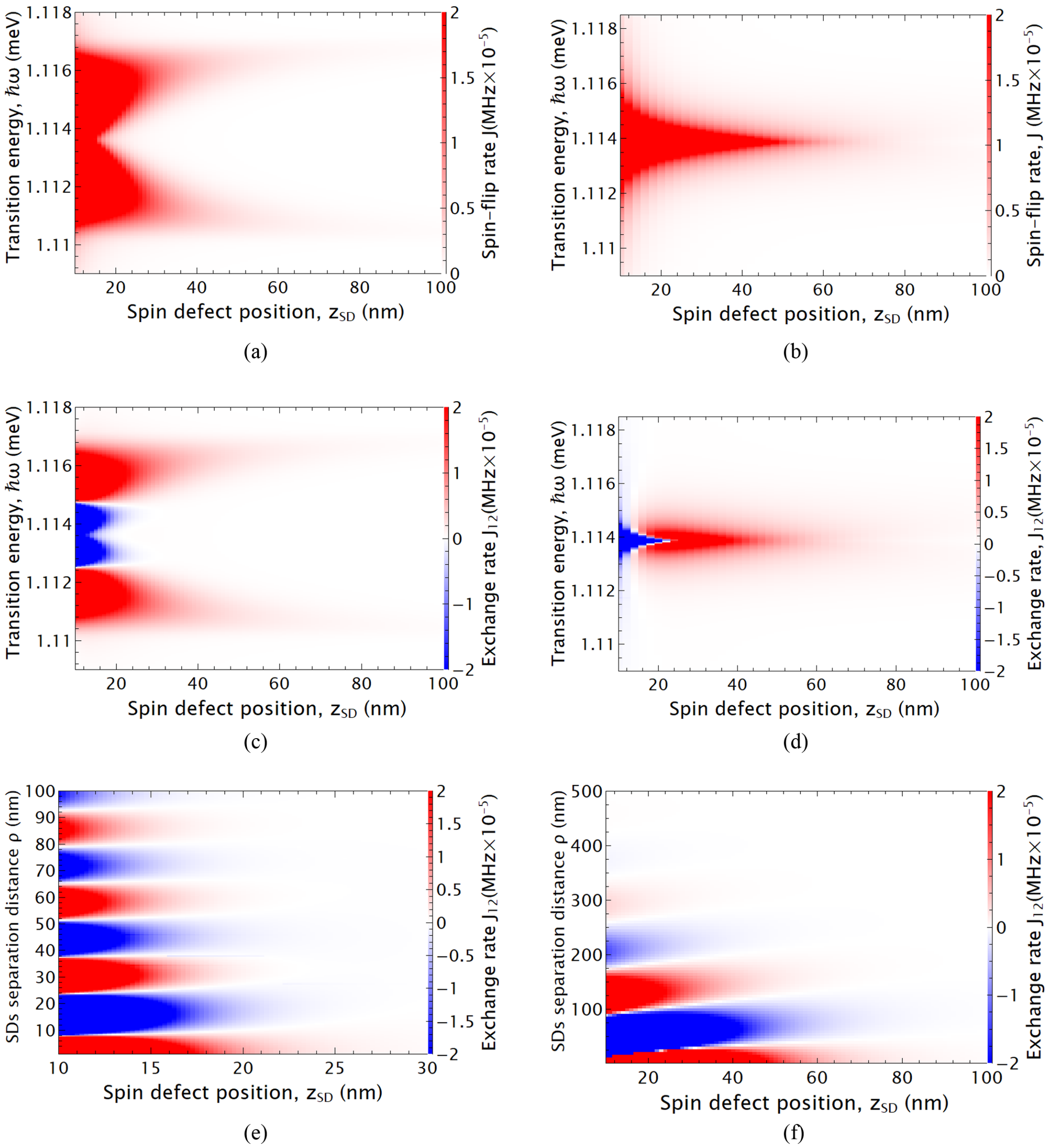

(a) (b) (c) (d) (e) (f)

FIG. 4. Contour plot of the spin-flip rate, J, of a single spin defect (SD) and the exchange interaction rate, J_{12}, between a pair of SDs, placed close to an antiferromagnetic (AFM) layer. We vary the emission energy and position of the SDs. Two different thicknesses are considered: (a),(c),(e) 10 nm and (b),(d),(f) 100 nm, for the AFM layer. The lateral separation distance between the pair of SDs is (c) $\rho = 15$ nm and (d) $\rho = 25$ nm. The emission energy is (e) $\hbar\omega_1 = 1.1135$ meV and (f) $\hbar\omega_1 = 1.113\,88$ meV.

fixed transition energy for the SDs and vary the separation distance from the AFM layer z_{SD} and the in-plane separation distance ρ. The transition energies of the SDs are (e) $\hbar\omega_1 = 1.1135m$ meV and (f) $\hbar\omega_1 = 1.113\,88$ meV. In Fig. 4(e) we observe that as the in-plane separation ρ between the SDs increases there are oscillations connected with the magnon polariton propagating wavelength along the AFM layer, which has a value $\lambda_{\mathrm{MP}} = 30$ nm; at the same time as the separation distance of the SDs from the AFM layers z_{SD} simultaneously increases the J_{12} value drops; this decrease is again connected with the penetration depth of the magnon polariton mode. For the thicker AFM layer, $D = 100$ nm, we again observe that the exchange rate J_{12} presents an oscillatory behavior with larger magnon polariton wavelength, $\lambda_{\mathrm{MP}} \sim 100$ nm, meaning a larger distance between the maxima and minima of J_{12}. Thus, the SDs can interact over larger distances along the AFM layer. Moreover, the thicker AFM layer supports magnon polariton modes with higher penetration depth, allowing SDs to interact over larger z_{SD}.

To fully describe the interaction between a pair of SDs the full spectra of the $J(\omega)$ and $J_{12}(\omega)$ are needed in the set of Eq. (14), although it is very common for these rates to be described by using Lorentzian fittings close to resonance peaks. From the spectra presented in Fig. 4 we clearly observe that this method is not valid for our case, since J_{12} supports multiple peaks and troughs accompanied with a sign change

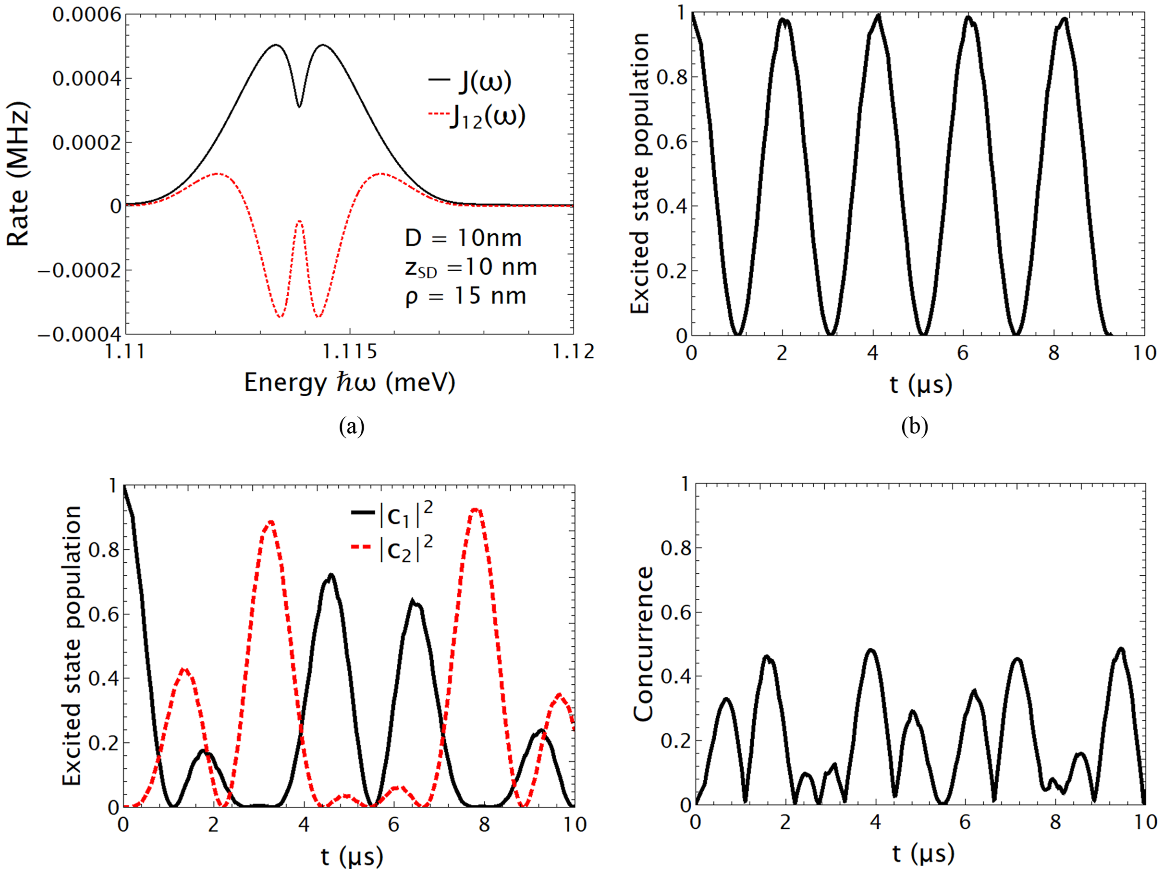

(a) (b)

(c) (d)

FIG. 5. (a) Spin-flip rate, $J(\omega)$, of a SD and exchange rate $J_{12}(\omega)$ for a pair of SDs that are 10 nm placed above a 10 nm AFM layer. (b) Population density of the excited state of a single SD. (c) Population probability of the excited states of a pair of SDs that are 15 nm apart and (d) value of the concurrence between the SDs.

as well. Furthermore, J and J_{12} do not have a Lorentzian profile. We consider a pair of SDs placed 10 nm away from an AFM layer of thickness of 10 nm. The separation distance between them, $\rho = 15$ nm, has been chosen because it is connected with the highest $|J_{12}| \simeq 0.0004$ MHz value for the transition energy of $\hbar\omega_1 = 1.1135$ meV, as can been seen in Fig. 5(a); the quality factor of the magnon resonance mode is $\omega_1/\Delta\omega_1 = 2700$. The strong-coupling regime appears as a coherent energy exchange between the SD and the AFM layer; in Fig. 5(b) we present the excited state population dynamics of a single SD where the characteristic Rabi oscillations are observed, where a close to a sinusoidal profile can be seen.

To apply quantum computing processes using the SD/AFM layer system we need to investigate the interaction between a pair of SDs that are the main components of the CNOT gate. Quantum computer systems surpass the capabilities of the conventional computer systems used in our everyday life for increasing problem sizes due to scaling, although it is extremely challenging to develop such devices. In Fig. 5(c) we consider the interaction between a pair of SDs which have been initialized to the state $|\psi(0)\rangle = |\uparrow_1, \downarrow_2, \{0\}_{\mathbf{r},\omega}\rangle$, where the SD 1 is at the excited state and, as the time evolves, exchange population with SD 2 through the magnon mode of the AFM layer. This effect can be clearly demonstrated through the degree of entanglement between the two SDs presented by the concurrence, which after the summation over the magnon modes is given by $C(t) = 2|c_1(t)c_2^*(t)|$, where c_1 and c_2 are given by Eqs.[14]; also check Appendix B [41,42]. The two SDs are entangled when the quantum state of each cannot be described independently of the state of the other; a completely entangled state is left invariant under the spin-flip operation, such that its projection to the initial state is 1, meaning the highest value of the concurrence is $C = 1$ and the lowest is $C = 0$. In Fig. 5(d) we observe that initially the two SDs are disentangled, and due to the interaction with the magnon mode of the AFM layer the C value increases, because the SDs exchange population. The high value of entanglement is persistent over long time spans reaching a value $C = 0.4$.

We now consider a thicker AFM layer, 100 nm, and in Fig. 6(a) we present the spin flip $J(\omega)$ and exchange rate $J_{12}(\omega)$ of SDs placed 10 nm away from the AFM layer and a separation distance of 25 nm. The transition energy of the SDs is $\hbar\omega_1 = 1.113\,88$ meV and we observe that both rates present a single peak value. Moreover, both rate values have been increased one order of magnitude for the $D = 100$ nm AFM thickness compared to the $D = 10$ nm; the reason is that for the thicker AFM layer there is a stronger coupling with the near field of the SDs. In Fig. 6(b) the population of the excited state of a single SD presents Rabi oscillations and the difference with the $D = 10$ nm is that the SD does

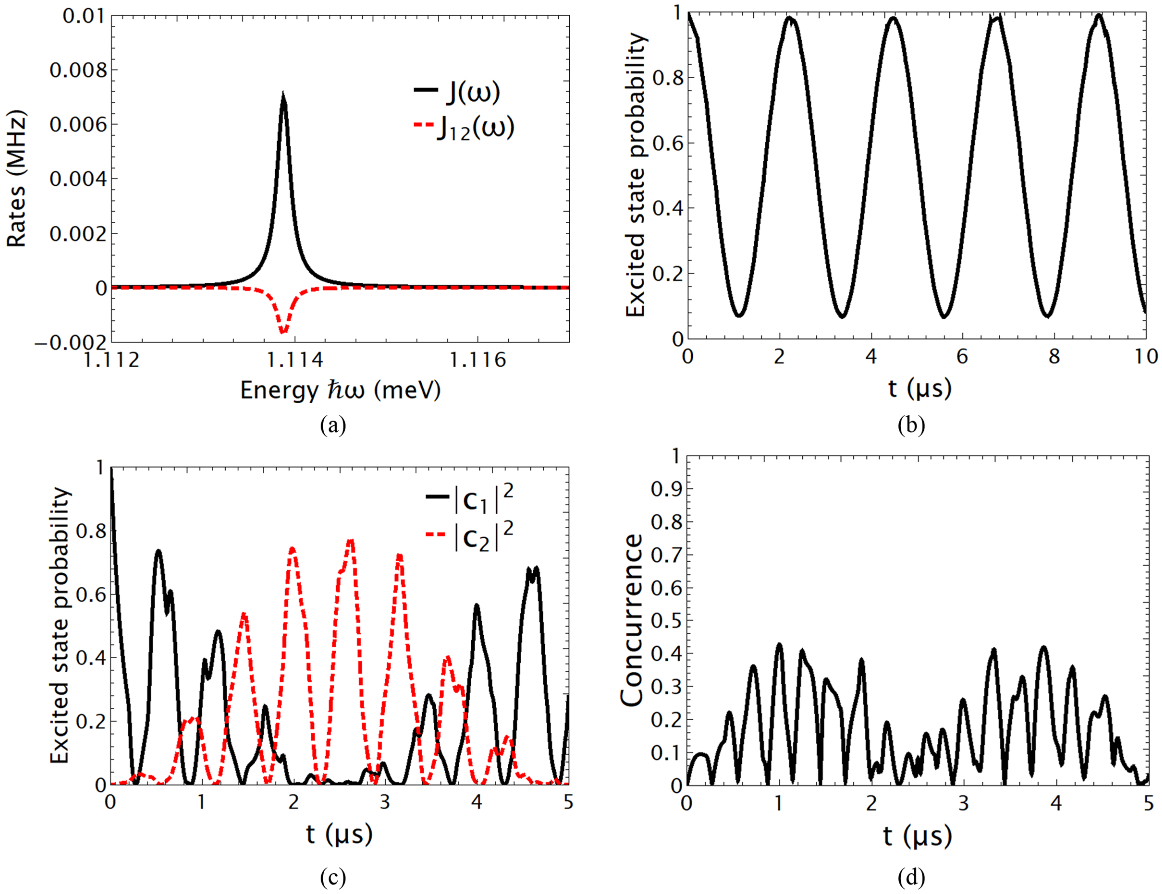
(a) (b) (c) (d)

FIG. 6. (a) Spectral density value of a spin defect that is placed above an antiferromagnetic layer, $J(\omega)$, for a single SD and $J_{12}(\omega)$ for a pair of SDs. (b) Population density of the excited state of the spin SD. (c) Population probability of the excited state of a pair of SDs and (d) value of the concurrence between the SDs. The AFM layer thickness is 100 nm, the SD/AFM layer separation is 10 nm, and the separation distance between them is 25 nm.

not fully relax to the ground state; this effect is attributed to the stronger SD/AFM layer interaction. When we consider the interaction between a pair of SDs, Fig. 6(c), we observe that they exchange population probability, showing a clear non-Markovian behavior. Again high entanglement between a pair of SDs is observed between a pair of SDs which is measured by the concurrence value in Fig. 6(d). Due to the stronger interaction between a pair of SDs for $D = 100$ nm, compared to $D = 10$ nm, the period of the oscillations is reduced meaning that more oscillations are observed on the same time span.

IV. CONCLUSIONS AND FUTURE WORK

We presented that the AFM MnF_2 layer can be used as a platform to achieve the strong light-matter interaction, where entanglement between two SDs is presented. The SDs interact through the magnon polariton modes supported by the AFM layer. The properties of the magnon polariton modes are characterized by the layer thickness, where the thicker AFM layers resemble the single dielectric/AFM material interface. Moreover, the magnon wavelength characterizes the interaction between the two SDs, as can be seen from Fig. 4.

Starting from the single SD/AFM layer interaction, a reversible dynamics is probed in the SD excited state population, $|c_1|^2$, which is a sign that the SD/AFM layer system operates in the strong-coupling regime. By placing a second SD in the vicinity of an initially excited SD, population exchange is observed. The interaction between the two SDs leads to a high degree of entanglement which is observed through studying the concurrence value $C(t)$.

The SDs are important elements for quantum sensing and computing applications. Thus, the exact theoretical modeling of their relaxation when placed close to an AFM layer is important. We use experimentally measured quantities to describe the electromagnetic response of the AFM layer. Moreover, the propagation wavelength of the magnon polariton mode of the thinner AFM layer can be used to potentially couple multiple SDs over smaller distances.

In particular, the AFM layer of $D = 10$ nm thickness presents a very interesting feature; the exchange rate J_{12} between a pair of SDs presents an oscillatory behavior, maintaining the maximum absolute value over multiple oscillation periods, three periods over 100 nm [see Fig. 4(e)], while for the AFM layer of thickness $D = 100$ nm after one period the coupling strength drops [see Fig. 4(f)]. Thus, the AFM layer of $D = 10$ nm thickness can be used to solve the problem of connectivity between multiple qubits, since each single SD can be coupled to multiple SDs. This will be the next step of our research.

ACKNOWLEDGMENTS

V.K. was supported by JSPS KAKENHI Grant No. JP21K13868 and No. JP22H01975.

APPENDIX

1. Intermediate steps to calculate the two spin-defect dynamics

We apply the Schrödinger equation at state $|\psi(t)\rangle$, Eq. (13), using the Hamiltonian of Eq. (2) and we extract the following system of equations that describe the excited state population of the two SDs:

$$\frac{dc_l(t)}{dt} = i\mu_0 \int d\mathbf{r}' \int d\omega \sqrt{-\frac{\hbar k_0}{\pi}\mathrm{Im}\mu(\mathbf{r}',\omega)^{-1}} \times C(\mathbf{r}',\omega,t)e^{-i(\omega-\omega_1)t}\mathfrak{J}(\mathbf{r}',\mathbf{r}_l,\omega), \tag{A1}$$

for $l = 1, 2$ for each of the SDs. The field density probability is given by the equation

$$\frac{dC(\mathbf{r},\omega,t)}{dt} = -i\sqrt{-\frac{\hbar}{\mu_0\pi}\mathrm{Im}\mu(\mathbf{r},\omega)^{-1}} \times [c_1(t)e^{i(\omega-\omega_1)t}\mathfrak{J}^*(\mathbf{r},\mathbf{r}_1,\omega) + c_2(t)e^{i(\omega-\omega_1)t}\mathfrak{J}^*(\mathbf{r},\mathbf{r}_2,\omega)]. \tag{A2}$$

After a few algebraic calculations we extract the system of the integrodifferential equations, Eq. (14) of the main part of the paper.

2. Quantum entanglement between two spin defects

The single-photon interaction between a pair of SDs is given by Eq. (13), where in $|1, 2, \text{field}\rangle$ the third entry describes the electromagnetic excitation in the system, and the first and second indices describe the ↑ or ↓ state of SDs 1 and 2, respectively. The density matrix of the two SDs in the basis $B = \{|1\rangle = |\uparrow,\uparrow\rangle,\ |2\rangle = |\uparrow,\downarrow\rangle,\ |3\rangle = |\downarrow,\uparrow\rangle,\ |4\rangle = |\downarrow\downarrow\rangle\}$, where again the first and second entries describe the state of the two SDs. Then the density matrix has the form

$$\hat{\rho} = \begin{pmatrix} \rho_{11} & 0 & 0 & \rho_{14} \\ 0 & \rho_{22} & \rho_{23} & 0 \\ 0 & \rho_{32} & \rho_{33} & 0 \\ \rho_{41} & 0 & 0 & \rho_{44} \end{pmatrix}; \tag{A3}$$

then we need to trace out the electromagnetic degrees of freedom from Eq. (13) over the basis B, through the expression

$$\hat{\rho}_A = \sum_{j=1}^{4} \langle j|_B|\psi(t)\rangle\langle\psi(t)||j\rangle_B, \tag{A4}$$

then the reduced density matrix has the form

$$\hat{\rho}_A = \begin{pmatrix} 0 & 0 & 0 & 0 \\ 0 & |c_1(t)|^2 & c_1(t)c_2^*(t) & 0 \\ 0 & c_1^*(t)c_2(t) & |c_1(t)|^2 & 0 \\ 0 & 0 & 0 & 1-|c_1(t)|^2-|c_2(t)|^2 \end{pmatrix}. \tag{A5}$$

The nondiagonal elements $\rho_{23} = \rho_{32}^* = c_1(t)c_2^*(t)$ describe the interaction and the subsequent exchange of population between the two SDs [41,42]. The level of entanglement can be described through the value of the concurrence C. Here we consider SD 1 to be initially excited; then the concurrence is given by the expression

$$C(t) = 2|c_1(t)c_2^*(t)|. \tag{A6}$$

The maximum possible entanglement between the two SDs is achieved when $C = 1$ and the two SDs are completely disentangled when $C = 0$.

3. Additional relations for the Green's tensor formalism of the antiferromagnetic layer

The

$$\mathbf{M}(\mathbf{k},\mathbf{r}) = i\mathbf{k}\times\hat{z}e^{i\mathbf{k}\cdot\mathbf{r}},\quad \mathbf{N}(\mathbf{k},\mathbf{r}) = i\frac{1}{k}\mathbf{k}\times\mathbf{k}\times\hat{z}e^{i\mathbf{k}\cdot\mathbf{r}} \tag{A7}$$

modes of the Green's tensor, Eq. (17), when inserted into the boundary conditions, Eqs. (18), satisfy the relations

$$\hat{z}\times\mathbf{M}(\mathbf{k},\mathbf{r}) = i\mathbf{k}_\rho e^{i\mathbf{k}\cdot\mathbf{r}}, \tag{A8a}$$

$$\hat{z}\times\mathbf{N}(\mathbf{k},\mathbf{r}) = \pm\frac{k_z}{k}\hat{z}\times\mathbf{k}_\rho e^{i\mathbf{k}\cdot\mathbf{r}}, \tag{A8b}$$

$$\hat{z}\times\vec{\mu}^{-1}\nabla\times\mathbf{M}(\mathbf{k},\mathbf{r}) = \pm\mu_x^{-1}k_z\hat{z}\times\mathbf{k}_\rho e^{i\mathbf{k}\cdot\mathbf{r}}, \tag{A8c}$$

$$\hat{z}\times\vec{\mu}^{-1}\nabla\times\mathbf{N}(\mathbf{k},\mathbf{r}) = i\mu_x^{-1}k\mathbf{k}_\rho\mathbf{e}^{\mathbf{ik\cdot r}}, \tag{A8d}$$

where $\mathbf{k} = (\mathbf{k}_\rho, k_z)$ and $\mathbf{k}_\rho = \mathbf{i}k_x + \mathbf{j}k_y$ is the in-plane wave vector. $\vec{\mu}$ is the magnetic permeability tensor, which for the case considered here is a diagonal matrix and is expressed as a vector; the AFM layer is the only magnetic material considered in this geometry.

To translate the Green's tensor $\mathfrak{G}$ to the $\mathfrak{J}$ tensor we use the $\mathfrak{J}(\mathbf{r},\mathbf{s},\omega) = \nabla_\mathbf{r}\times\nabla_\mathbf{s}\times\mathfrak{G}(\mathbf{r},\mathbf{s},\omega)$ expression, where the relations

$$\nabla\times\mathbf{M}(\mathbf{k},\mathbf{r}) = k\mathbf{N}(\mathbf{k},\mathbf{r}), \tag{A9a}$$

$$\nabla\times\mathbf{N}(\mathbf{k},\mathbf{r}) = k\mathbf{M}(\mathbf{k},\mathbf{r}) \tag{A9b}$$

hold [37].

---

[1] R. Macêdo and T. Dumelow, Tunable all-angle negative refraction using antiferromagnets, Phys. Rev. B **89**, 035135 (2014).

[2] J. Sloan, N. Rivera, J. D. Joannopoulos, I. Kaminer, and M. Soljacic, Controlling spins with surface magnon polaritons, Phys. Rev. B **100**, 235453 (2019).

[3] D. Kikuchi, D. Prananto, K. Hayashi, A. Laraoui, N. Mizuochi, M. Hatano, E. Saitoh, Y. Kim, C. A. Meriles, and T. An, Long-distance excitation of nitrogen-vacancy centers in diamond via surface spin waves, Appl. Phys. Express **10**, 103004 (2017).

[4] T. X. Zhou, J. J. Carmiggelt, L. M. Gächter, I. Esterlis, D. Sels, R. J. Stohr, C. Du, D. Fernandez, J. F. Rodriguez-Nieva, F. Buttner, E. Demler, and A. Yacoby, A magnon scattering platform, Proc. Natl. Acad. Sci. USA **118**, e2019473118 (2021).

[5] D. Prananto, Y. Kainuma, K. Hayashi, N. Mizuochi, K.-i. Uchida, and T. An, Probing Thermal Magnon Current Mediated by Coherent Magnon via Nitrogen-Vacancy Centers in Diamond, Phys. Rev. Appl. **16**, 064058 (2021).

[6] X. Wang, Y. Xiao, C. Liu, E. Lee-Wong, N. J. McLaughlin, H. Wang, M. Wu, H. Wang, E. E. Fullerton, and C. R. Du, Electrical control of coherent spin rotation of a single-spin qubit, npj Quantum Inf. **6**, 78 (2020).

[7] Y. Tabuchi, S. Ishino, T. Ishikawa, R. Yamazaki, K. Usami, and Y. Nakamura, Hybridizing Ferromagnetic Magnons and Microwave Photons in the Quantum Limit, Phys. Rev. Lett. **113**, 083603 (2014).

[8] Y. Tabuchi, S. Ishino, A. Noguchi, T. Ishikawa, R. Yamazaki, K. Usami, and Y. Nakamura, Coherent coupling between a ferromagnetic magnon and a superconducting qubit, Science **349**, 405 (2015).

[9] Y. Tabuchi, S. Ishino, A. Noguchi, T. Ishikawa, R. Yamazaki, K. Usami, and Y. Nakamura, Quantum magnonics: The magnon meets the superconducting qubit, C. R. Phys. **17**, 729 (2016).

[10] D. Lachance-Quirion, Y. Tabuchi, A. Gloppe, K. Usami, and Y. Nakamura, Hybrid quantum systems based on magnonics, Appl. Phys. Express **12**, 070101 (2019).

[11] C. C. Rusconi, M. J. A. Schuetz, J. Gieseler, M. D. Lukin, and O. Romero-Isart, Hybrid architecture for engineering magnonic quantum networks, Phys. Rev. A **100**, 022343 (2019).

[12] A. Rustagi, I. Bertelli, T. van der Sar, and P. Upadhyaya, Sensing chiral magnetic noise via quantum impurity relaxometry, Phys. Rev. B **102**, 220403(R) (2020).

[13] B. Flebus, H. Ochoa, P. Upadhyaya, and Y. Tserkovnyak, Proposal for dynamic imaging of antiferromagnetic domain wall via quantum-impurity relaxometry, Phys. Rev. B **98**, 180409(R) (2018).

[14] B. Flebus and Y. Tserkovnyak, Quantum-Impurity Relaxometry of Magnetization Dynamics, Phys. Rev. Lett. **121**, 187204 (2018).

[15] Y.-Y. Lai, G.-D. Lin, J. Twamley, and H.-S. Goan, Single-nitrogen-vacancy-center quantum memory for a superconducting flux qubit mediated by a ferromagnet, Phys. Rev. A **97**, 052303 (2018).

[16] A. B. Solanki, S. I. Bogdanov, M. M. Rahman, A. Rustagi, N. R. Dilley, T. Shen, W. Tong, P. Debashis, Z. Chen, J. Appenzeller, Y. P. Chen, V. M. Shalaev, and P. Upadhyaya, Electric field control of interaction between magnons and quantum spin defects, Phys. Rev. Res. **4**, L012025 (2022).

[17] C. Gonzalez-Ballestero, T. van der Sar, and O. Romero-Isart, Phys. Rev. B **105**, 075410 (2022).

[18] P. E. Dolgirev, S. Chatterjee, I. Esterlis, A. A. Zibrov, M. D. Lukin, N. Y. Yao, and E. Demler, Characterizing two-dimensional superconductivity via nanoscale noise magnetometry with single-spin qubits, Phys. Rev. B **105**, 024507 (2022).

[19] M. Fukami, D. R. Candido, D. D. Awschalom, and M. E. Flatte, Opportunities for long-range magnon-mediated entanglement of spin qubits via on- and off-resonant coupling, PRX Quantum **2**, 040314 (2021).

[20] L. Trifunovic, F. L. Pedrocchi, and D. Loss, Long-Distance Entanglement of Spin Qubits via Ferromagnet, Phys. Rev. X **3**, 041023 (2013).

[21] B. Flebus and Y. Tserkovnyak, Entangling distant spin qubits via a magnetic domain wall, Phys. Rev. B **99**, 140403(R) (2019).

[22] J. Zou, S. K. Kim, and Y. Tserkovnyak, Tuning entanglement by squeezing magnons in anisotropic magnets, Phys. Rev. B **101**, 014416 (2020).

[23] J. Zou, S. Zhang, and Y. Tserkovnyak, Bell-state generation for spin qubits via dissipative coupling, Phys. Rev. B **106**, L180406 (2022).

[24] T. Neuman, D. S. Wang, and P. Narang, Nanomagnonic Cavities for Strong Spin-Magnon Coupling and Magnon-Mediated Spin-Spin Interactions, Phys. Rev. Lett. **125**, 247702 (2020).

[25] D. S. Wang, T. Neuman, and P. Narang, Spin emitters beyond the point dipole approximation in nanomagnonic cavities, J. Phys. Chem. C **125**, 6222 (2021).

[26] W. Xiong, M. Tian, G.-Q. Zhang, and J. Q. You, Strong long-range spin-spin coupling via a Kerr magnon interface, Phys. Rev. B **105**, 245310 (2022).

[27] S. Scheel and S. Y. Buhmann, Macroscopic Quantum Electrodynamics—Concepts and Applications, Acta Phys. Slovaca 58, 675 (2009), arXiv:0902.3586.

[28] K. Head-Marsden, J. Flick, C. J. Ciccarino, and P. Narang, Quantum information and algorithms for correlated quantum matter, Chem. Rev. **121**, 3061 (2021).

[29] N. Rivera and I. Kaminer, Light-matter interactions with photonic quasiparticles, Nat. Rev. Phys. **2**, 538 (2020).

[30] S. M. Rezende, A. Azevedo, and R. L. Rodriguez-Suarez, Introduction to antiferromagnetic magnons, J. Appl. Phys. **126**, 151101 (2019).

[31] K. Abraha and D. R. Tilley, Theory of far infrared properties of magnetic surfaces, films and superlattices, Surf. Sci. Rep. **24**, 129 (1996).

[32] M. Lui, C. A. Ramos, A. R. King, and V. Jaccarino, Antiferromagnetic standing-spin-wave resonance in epitaxial films of $\mathrm{MnF_2}$, J. Appl. Phys. **67**, 5518 (1990).

[33] T. Dumelow and M. C. Oliveros, Continuum model of confined magnon polaritons in superlattices of antiferromagnets, Phys. Rev. B **55**, 994 (1997).

[34] C. Henkel, S. Potting, and M. Wilkens, Loss and heating of particles in small and noisy traps, Appl. Phys. B **69**, 379 (1999).

[35] C. Henkel and M. Wilkens, Heating of trapped atoms near thermal surfaces, Europhys. Lett. **47**, 414 (1999).

[36] B. A. Ferreira and N. M. R. Peres, The magnetic Purcell effect: The case of an emitter near an antiferromagnet, Europhys. Lett. **127**, 37002 (2019).

[37] P. K. Rekdal, S. Scheel, P. L. Knight, and E. A. Hinds, Thermal spin flips in atom chips, Phys. Rev. A **70**, 013811 (2004).

[38] K. Y. Guslienko and A. N. Slavin, Magnetostatic Green's functions for the description of spin waves in finite rectangular magnetic dots and stripes, J. Magn. Magn. Mater. **323**, 2418 (2011).

[39] I. Thanopulos, V. Karanikolas, N. Iliopoulos, and E. Paspalakis, Non-Markovian spontaneous emission dynamics of a quantum emitter near a MoS_2 nanodisk, Phys. Rev. B **99**, 195412 (2019).

[40] C.-J. Yang, J.-H. An, and H.-Q. Lin, Signatures of quantized coupling between quantum emitters and localized surface plasmons, Phys. Rev. Res. **1**, 023027 (2019).

[41] S. Maniscalco, F. Francica, R. L. Zaffino, N. Lo Gullo, and F. Plastina, Protecting Entanglement via the Quantum Zeno Effect, Phys. Rev. Lett. **100**, 090503 (2008).

[42] R. L. Franco, B. Bellomo, S. Maniscalco, and G. Compagno, Dynamics of quantum correlations in two-qubit systems within non-Markovian environments, Int. J. Mod. Phys. B **27**, 1345053 (2013).